International Journal of Nanomedicine

Dovepress
Taylor & Francis Group

Open Access Full Text Article

ORIGINAL RESEARCH

Multimodal Imaging-Guided Tumor Microenvironment-Responsive Nanoplatform for Synergistic Therapy of Pancreatic Cancer

Na Li[1,2,*], Haifeng Hu[2,*], Yuqi Li[3], Silong Li[3], Guangyue Shi[1], Xiaoyang Yu[1], Liguo Hao[1]

[1]Department of Molecular Imaging, School of Medical Technology, Qiqihar Medical University, Qiqihar, Heilongjiang, 161006, People's Republic of China; [2]Department of Imaging Medicine and Nuclear Medicine, School of Clinical Medicine, Jiamusi University, Jiamusi, Heilongjiang, 154002, People's Republic of China; [3]Medical Imaging, School of Medical Technology, Qiqihar Medical University, Qiqihar, Heilongjiang, 161006, People's Republic of China

*These authors contributed equally to this work

Correspondence: Liguo Hao, Department of Molecular Imaging, School of Medical Technology, Qiqihar Medical University, No. 333, Bukui North Street, Jianhua District, Qiqihar, Heilongjiang, 161006, People's Republic of China, Email haoliguo@qmu.edu.cn

Purpose: Chemotherapy remains an effective treatment for pancreatic cancer. However, the limitations of single-modal therapies and the absence of imaging-based monitoring during treatment pose challenges for real-time optimization of drug delivery, resulting in suboptimal therapeutic outcomes.

Methods: This study aims to design and develop a novel nanoparticle drug delivery system, HMP-ICG&DOX, which incorporates indocyanine green (ICG) as an FDA-approved near-infrared photothermal agent and doxorubicin (DOX) as a commonly used chemotherapeutic drug. The modification with NH_2-PEG-NH_2 enhances the biocompatibility of the nanocarrier. The designed nanoprobe exhibits the following features: (1) It decomposes in the tumor microenvironment (TME) to release Mn^{2+} for magnetic resonance T_1 imaging, while ICG provides near-infrared fluorescence imaging capabilities. (2) It facilitates synergistic photothermal-chemotherapy, significantly improving therapeutic efficacy against pancreatic cancer. (3) The pH-responsive drug release enhances drug utilization efficiency while minimizing side effects.

Results: Experimental results demonstrate that HMP-ICG&DOX nanoparticles possess excellent biocompatibility, antitumor activity, controlled drug release, and multimodal imaging tracking abilities.

Conclusion: In conclusion, the HMP-ICG&DOX nanoparticles designed in this study offer promising applications in the diagnosis and treatment of pancreatic cancer.

Keywords: pancreatic cancer, magnetic resonance imaging, hollow manganese dioxide, indocyanine green, adriamycin

Introduction

Pancreatic cancer is a malignant tumor of the digestive system that is challenging to diagnose at an early stage and is associated with a very poor prognosis, characterized by a five-year survival rate of less than 10%.[1,2] Currently, commonly used clinical imaging methods, such as enhanced CT and MRI, can detect pancreatic lesions; however, their sensitivity for early, small lesions (less than 2 cm) is insufficient, ranging only from 60% to 75%. This limitation may result in misdiagnosis or missed diagnoses.[3–5] Currently, the primary treatments for pancreatic cancer encompass surgical resection, radiotherapy, and chemotherapy. However, the unique anatomical structure, invasiveness, rapid metastasis, and drug resistance associated with pancreatic cancer contribute to a low rate of surgical resection and unsatisfactory outcomes from chemotherapy.[6–9] Consequently, there is an urgent need to develop novel diagnostic and therapeutic strategies for pancreatic cancer.

Nanocarriers have shown great potential in tumor diagnosis and therapy due to their unique size effects and highly customizable functional properties.[10–13] Hollow nanocarriers can be loaded with chemotherapeutic agents or photothermal converters to facilitate targeted delivery, thereby reducing off-target toxicity. Additionally, they possess the capability to integrate multimodal imaging and therapy, which enables precise and real-time monitoring of the lesion site during treatment.[14,15]

Received: 25 May 2025
Accepted: 3 November 2025
Published: 14 November 2025

Constructing nanoplatforms that incorporate efficient targeting, multimodal therapy, and biodegradability represents a significant strategy to enhance the effectiveness of diagnosis and treatment for pancreatic cancer. In recent years, hollow manganese dioxide has emerged as a prominent research focus in drug delivery systems, owing to its degradability and properties suitable for magnetic resonance imaging.[16–19] Hollow manganese dioxide is a prominent candidate in cancer therapy and diagnostics due to its ability to decompose into non-toxic, water-soluble Mn^{2+} in the body, which can be rapidly excreted through renal metabolism, thereby mitigating the risk of long-term in vivo toxicity accumulation. Liu et al were the first to design poly(ethylene glycol)-modified hollow manganese dioxide nanoparticles for tumor therapy. This innovative approach integrates multimodal diagnostic and therapeutic functions with the capacity to regulate the tumor microenvironment, significantly enhancing the synergistic antitumor efficacy of the nanoparticles.[20] The Zhang research group has successfully developed a hollow mesoporous manganese dioxide-based nanoplatform (M-HMnO_2@ICG) for multimodal imaging-guided photodynamic and chemodynamic therapy. This platform exhibits excellent responsive degradation properties within the tumor microenvironment, enabling efficient loading and release of ICG. Simultaneously, it enhances photodynamic therapy (PDT) and chemodynamic therapy (CDT) efficacy through autocatalytic oxygen generation and glutathione (GSH) consumption.[21]

Photothermal therapy (PTT) is a non-invasive tumor treatment with the advantages of low drug resistance, low trauma, and good tissue selectivity.[22–25] During PTT, the precise irradiation of near-infrared light excites photothermal converters that are enriched in the tumor lesion area. By irradiating near-infrared light, photothermal conversion agents enriched in tumor lesions are excited to convert light energy into heat energy, causing irreversible thermal damage to tumor cells, and finally achieving complete ablation of the tumor and achieving the exact treatment purpose.[26–28] Studies have shown that local hyperthermia can not only directly damage the physiological structure and function of tumor cells, but also significantly enhance the uptake and sensitivity of tumor cells to chemotherapy drugs, which provides the possibility of synergistic therapy.[29,30] ICG is a near-infrared photothermal conversion agent approved by the Food and drug administration (FDA) with excellent photothermal conversion efficiency.[31] However, it is prone to aggregation and quenching in vivo, and its short half-life, usually only 2–4 min, results in its low effective retention rate in tumor tissues, which limits its application.[32] At the same time, DOX, as a broad-spectrum anthracycline chemotherapeutic agent, has an inhibitory effect on a variety of tumors, but its clinical application is seriously limited by cardiotoxicity and Multidrug resistance (MDR).[33–36] Although previous studies have attempted to co-deliver DOX and ICG using liposomes and other nanocarriers.[33] However, these systems are often limited by the inherent defects of a single treatment mode, and lack of effective integration of real-time imaging monitoring systems, which leads to the inability to dynamically optimize parameters according to feedback during treatment.[37–40] Therefore, there is an urgent need to develop a nano-platform that can stably load ICG, realize PTT-chemotherapy collaborative treatment, and integrate real-time image monitoring functions to overcome the above challenges.

To address the aforementioned issues, this study designed and constructed hollow manganese dioxide-based nanoparticles, HMP-ICG&DOX NPs. This platform utilizes NH_2-PEG-NH_2-modified HMP as a carrier, co-loading DOX and ICG through electrostatic adsorption. It optimizes the biosafety of conventional hollow manganese dioxide while enabling pH-responsive drug release, overcoming the limitations of DOX and ICG to achieve synergistic chemo-photothermal therapy. Within the tumor microenvironment, the HMP shell degrades to release Mn^{2+}, DOX, and ICG. Mn^{2+} enhances T_1-weighted MRI signals for real-time drug distribution monitoring. ICG generates localized hyperthermia under 808 nm laser irradiation, directly killing tumor cells while promoting DOX penetration and inducing apoptosis, ultimately achieving synergistic chemo-photothermal therapy. In vitro and in vivo experiments demonstrate that this nano system effectively penetrates the pancreatic cancer stromal barrier, significantly inhibits tumor growth, and exhibits excellent biosafety. This study overcomes the limitations of traditional carriers' disjointed "imaging-therapy" approaches, providing a novel technological platform for real-time monitoring during the early diagnosis and treatment of pancreatic cancer.

Materials and Methods

Reagents

Tetraethoxysilane (TEOS, 99%), polyallylamine hydrochloride (PAH), 1-(3-dimethylaminopropyl)-3-ethylcarbodiimide (EDC), sodium carbonate (Na_2CO_3), ammonia (NH_3-H_2O), polyacrylic acid (PAA), indocyanine green (ICG), doxorubicin (DOX), and N-hydroxysuccinimide (NHS) were from Aladdin. Potassium permanganate ($KMnO_4$), 4% paraformaldehyde from Sinopharm.

Cell Counting Kit-8, DAPI staining solution from Biotronik. RPMI 1640 cell culture medium, DMEM cell culture medium, penicillin-streptomycin from Corning. Pancreatic cell digest and fetal bovine serum from Gibco.

Preparation of HMP NPs

Solid silica ($sSiO_2$) nanoparticles were synthesized according to methods previously reported in the literature.[41,42] To be 140 mL of anhydrous ethanol, 20 mL of deionized water and 5 mL of ammonia were mixed and stirred at 45 °C for 30 min and then TEOS was added drop by drop, and the reaction was continued for 3 h. The white $sSiO_2$ solid was obtained by centrifugation, washed with anhydrous ethanol and dried. Subsequently, 300 mg $KMnO_4$ was dissolved by ultrasonication, and $sSiO_2$ aqueous solution was added drop by drop with ultrasonication and shaking for 6 h. Centrifugation was performed to wash the supernatant without purple color to obtain $sSiO_2@MnO_2$. It was reacted with 2 M Na_2CO_3 solution at 60 °C for 12 h and lyophilized by centrifugation to obtain HM NPs. HMP NPs were further modified by PAH and PAA and then activated by EDC/NHS to connect NH_2-PEG-NH_2, and finally washed by centrifugation to obtain HMP NPs.

Preparation of HMP-ICG&DOX NPs

Weigh 3 mg of ICG and 3 mg of DOX dissolved in 5 mL of deionized water, ultrasonically shaking and mixing, add 15 mg of HMP NPs, and stirring under the condition of light-avoidance for 24 h to obtain the HMP-ICG&DOX NPs.

Material Characterization

Sample morphology and elemental composition were examined using scanning electron microscopy (SEM, ZEISS Sigma 300), transmission electron microscopy (TEM, FEI Tecnai F20), and X-ray energy dispersive spectroscopy (EDS, Oxford X-Max 80 T). The particle size and zeta potential of the samples were characterized with a Malvern nanoparticle sizer (Nano-ZS90). The elemental valence states of the samples were analyzed via X-ray photoelectron spectroscopy (XPS, Shimadzu/Krayos AXIS Ultra DLD). The crystal structures of the HM nanoparticles were assessed through X-ray diffraction (XRD, Panalytical XPert3). Specific surface area and pore structure were determined using a specific surface area and porosity analyzer (BET, Micromeritics 3Flex). The UV-visible-near-infrared spectra of the samples were recorded with a UV spectrophotometer (UV-1285, Shimadzu). Raman spectra were obtained using a Raman spectrometer (Horiba LabRAM Odyssey). Furthermore, the in vitro imaging properties of the nanoparticles were validated using a 3.0 T magnetic resonance imaging system (Philips).

Stability of Nanoparticles

To assess the stability of the nanoparticles, HMP NPs (500 μg/mL) were dispersed in deionized water (ddH_2O), RPMI 1640 and saline (0.9% NaCl), and were photographed for before-and-after comparative analyses after 24 h of standing. In addition to this, dynamic light scattering measurements were performed for each type of sample on 5 consecutive days.

Detection of Drug Load (DL%) and Encapsulation Efficiency (EE%)

The 1 mg/mL ICG master batch and DOX master batch were prepared separately, and the gradient dilution was carried out using deionized water to obtain 1, 2, 4, 8, 16 μg/mL ICG standard solutions and 2, 4, 8, 16, 32 μg/mL DOX standard solutions. The absorbance of each concentration of standard solution was measured at 780 nm and 480 nm, respectively, and the standard curve was established.[43] After the reaction of HMP-ICG&DOX NPs, the resulting reaction mixture was centrifuged to separate the supernatant and precipitate. The content of ICG and DOX in HMP-ICG&DOX NPs was determined by UV spectrophotometer, and the drug loading (DL%) and encapsulation efficiency (EE%) were calculated according to the following formula:

$$\mathrm{DL}(\%)=\frac{\text{weight of the drug in NPs}}{\text{weight of NPs}}\times 100\%$$

$$\mathrm{EE}(\%)=\frac{\text{weight of the drug in NPs}}{\text{weight of the drug in feed}}\times 100\%$$

 https://doi.org/10.2147/IJN.S542677

Degradation and in vitro Drug Release Studies

The HMP NPs were incubated with PBS at different pH values (5.5, 6.8and 7.4), respectively, and the solutions were characterized by TEM at the given time points. Three dialysis bags containing HMP-ICG&DOX solution (5 mL, 1 mg/mL) were prepared for suspension in PBS buffer at pH 5.5, 6.8 and 7.4, respectively, and then placed in a constant temperature shaker at 37 °C with 100 rpm shaking. We sampled 1 mL at 2, 4, 6, 8, 12, 24, and 48 h, while supplementing 1 mL of fresh release medium. The absorbance of each sample was determined using a UV spectrophotometer, and the concentration was calculated according to the standard curve equations for DOX and ICG, and the cumulative release rate of the drug was calculated according to the following equation:

$$\text{The drug release percentage}(\%)=\frac{V\times C_n+\sum_1^{n-1} C_k\times V_0}{m}\times 100\%$$

Where C_n represents the drug concentration in the release medium at the nth moment, V represents the overall volume of the release medium, C_k represents the drug concentration in the release medium at the kth moment, and V_0 is the volume of the sample removed at each time point.

In vitro Photothermal Performance Analysis

To validate the photothermal performance of nanoparticles, the photothermal properties of ddH_2O, Free DOX, Free ICG, HMP, and HMP-ICG&DOX NPs were evaluated using an infrared thermal imaging system under 10 min irradiation with an 808 nm laser (1 W/cm^2). Subsequently, the concentration dependence (12.5, 25, 50, 100 and 125 μg/mL) and power density dependence (0.5, 0.75, 1.0 and 1.5 W/cm^2) of HMP-ICG&DOX NPs were systematically analyzed. Photothermal stability was then evaluated for HMP-ICG&DOX NPs and Free ICG (both at 12.16 μg/mL ICG concentration) through five laser-on/natural-cooling cycles. The temperature change of the samples was recorded every 30s. Additionally, the photothermal conversion efficiencies of HMP-ICG&DOX NPs and Free ICG (both with an ICG concentration of 12.16 μg/mL) were calculated separately using the following formula:

$$\eta=\frac{hA\left(T_{max}-T_{sur}\right)-Qs}{I\left(1-10^{-A_\lambda}\right)}$$

Here, η is the heat transfer coefficient, A is the surface area of the container, T_{max} is the maximum temperature of HMP-ICG&DOX NPs, T_{sur} is the ambient temperature, Qs is the solvent absorption power, I is the laser power (1 W/cm^2), and A_λ is the absorbance of HMP-ICG&DOX NPs at 808 nm.

Evaluation of the Effects of Magnetic Resonance Imaging

To determine the relaxation rate of HMP-ICG&DOX NPs and to evaluate their magnetic resonance imaging capability, the concentration of Mn^{2+} was determined by inductively coupled plasma mass spectrometry (ICP-MS) to be 436.408 mg/L. The HMP-ICP&DOX NPs were then dispersed in PBS buffers with different Mn^{2+} concentrations (0.085–1.36 mM) in pH values of 5.5 and 7.4 in PBS buffers. After 4 h of incubation, MRI studies were performed using a 3.0 T magnetic resonance equipment and the relaxation rate was recorded by a 0.5 T NMI20 Analyst NMR system.

Cell Culture

Human pancreatic cancer cell line SW1990 and normal human pancreatic ductal endothelial cell line HPDE6C7 were obtained from the Shanghai Cell Bank, part of the Chinese Academy of Sciences. These cells were maintained in 1640 culture medium supplemented with 10% fetal bovine serum and 1% penicillin/streptomycin, or alternatively in high-glucose DMEM.

Biocompatibility of HMP NPs

The cellular safety of HMP NPs on HPDE6C7 and SW1990 cells was assessed using the CCK-8 assay. Both cell types were seeded in 96-well plates at a density of 6000 cells per well and incubated overnight at 37°C. HMP NPs were co-incubated with the cells at concentrations of 6.25, 12.5, 25, 50, 100, and 200 μg/mL for 24 h. Following this incubation period, the medium

was removed, and the incubation was continued by adding 10 μL of CCK-8 solution to each well for an additional 2 h. The absorbance of each well was then measured at 450 nm using a multifunctional enzyme marker.

The hemolysis test was conducted to assess the hemocompatibility of the materials. Fresh blood (1 mL) was collected and centrifuged at 4°C and 2000 rpm for 10 min, followed by three washes with saline to prepare an erythrocyte suspension. The diluted erythrocytes were co-incubated with saline (as a negative control), deionized water (as a positive control), and varying concentrations of HMP nanoparticles for 4 h. After incubation, the samples were centrifuged at 12,000 rpm for 10 min, and the absorbance values were measured at 540 nm using an enzyme marker. The percentage of hemolysis was calculated using the following formula:

$$\text{Hemolysis}\ (\%) = \frac{A_{\text{sample}} - A_{\text{negative control}}}{A_{\text{positive control}} - A_{\text{negative control}}} \times 100\%$$

We used female BALB/c nude mice as model animals to determine the in vivo toxicity of HMP NPs. A high dose (20 mg/kg) of HMP NPs or saline was injected into the tail vein. 7 days later, the liver and kidney functional indices of the model mice were examined in each group, and the model mice were necropsied to remove the major organs for histopathological examination.

In vitro Cellular Uptake Assay

SW1990 cells in the logarithmic growth phase (1×10^5 cells per well) were initially inoculated into confocal dishes and cultured overnight to ensure cell adherence to the dish surface. The experiment was divided into two groups: Experimental Group 1: Incubated for 4 h with 1 mL each of HMP-ICG&DOX NPs, Free DOX, and PBS buffer solution. The amount of DOX in the nanoparticle group was equivalent to that in the Free DOX group. Experimental Group 2 consisted of adding 1 mL of HMP-ICG&DOX NPs to the confocal petri dish, which was incubated under light protection for 0, 1, 2, and 4 h. Cells were then fixed in 4% paraformaldehyde for 20 min and subsequently incubated in DAPI solution for an additional 10 min. Finally, the cellular uptake in each group was observed using a confocal microscope.

Additionally, SW1990 cells (1.5×10^5 cells per well) were inoculated into six-well plates to facilitate adherence. HMP-ICG&DOX NPs were added and incubated in the dark for 0, 1, 2, and 4 h. Fluorescence intensity was measured using flow cytometry.

In vitro Cytotoxicity Assay

Cells were co-incubated in 96-well plates with a variety of treatments, including Free DOX, HMP-DOX, HMP-ICG combined with laser exposure, and HMP-ICG and DOX with laser exposure, over a duration of 24 h. After 4 h of drug incubation, cells were washed with PBS to remove excess nanoparticles, and fresh medium was added to the wells. Following this, the sample wells received irradiation from an 808 nm near-infrared (NIR) laser aimed at a power output of 1 W/cm^2 for a duration of 4 min. Upon completing the incubation process, 10 microliters of CCK-8 solution were added to each well to facilitate further incubation for an additional 2 h. This step is crucial for assessing cell viability and proliferation. The absorbance of the contents in the wells was subsequently measured using a multifunctional enzyme marker at a wavelength of 450 nm. The Combination Index (CI) was calculated using the Chou-Talalay method,[44] where CI > 1 indicates antagonism, CI = 1 denotes additive effects, and CI < 1 signifies synergistic effects. Cell activity was calculated using the following formula:

$$\text{Cell viability}(\%) = \frac{OD_{\text{sample}} - OD_{\text{blank}}}{OD_{\text{control}} - OD_{\text{blank}}} \times 100\%$$

In vitro Apoptosis Assay

The evaluation of apoptosis induction in SW1990 cells was conducted using HMP-ICG&DOX nanoparticles, with flow cytometry serving as the analytical method. This investigation established five distinct groups: PBS, Free DOX, HMP-DOX, HMP-ICG+Laser, and HMP-ICG&DOX+Laser. SW1990 cells were plated in 6-well dishes and allowed to adhere overnight. Subsequently, 2 mL of a filtered and sterilized sample solution was introduced into each well and incubated for 24 h. The collected cells were washed with PBS and resuspended in 500 μL of Binding Buffer solution, to which 5 μL of

Annexin V-FITC solution and 5 μL of Propidium Iodide solution were added. After incubating in the dark at room temperature for 10 min, flow cytometry was utilized to evaluate apoptosis.

Animal and Tumor Models

Female nude mice of the BALB/c strain were obtained from Liaoning Changsheng Biotechnology Co. The Animal Ethics Committee of Qiqihar Medical College approved all animal experiments (QMU-AECC-2024-152). Pre-feeding was conducted in a specific pathogen-free environment, maintaining stable temperature (22±1 °C) and humidity levels (50–60%). SW1990 cells were harvested and suspended in saline, and the concentration was modified to 1.0×10^7 cells/mL following cell counting. Subsequently, the nude mice were anesthetized, and a 100 μL cell suspension was injected subcutaneously into the axillary regions. Notable subcutaneous tumor nodules became evident after one week. Experiments continued once the tumor volume approximated 100 mm^3.

In vivo Fluorescence Imaging

Model mice were injected with 100 μL of HMP-ICG&DOX NPs and free ICG via the tail vein, respectively, with the same amount of ICG in both (5 mg/kg), and the in vivo fluorescence images of the model mice were observed using a small-animal in vivo fluorescence imaging system at 2 h, 4 h, 6 h, 8 h, 12 h, and 24 h after the injection of the drugs. The model mice were put to death 24 h later to remove the major organs and tumor tissues, washed with PBS and subjected to fluorescence imaging. Additionally, the content of manganese ions in visceral tissues was determined using inductively coupled plasma mass spectrometry (ICP-MS).

In vivo Magnetic Resonance Imaging

SW1990 model mice were subjected to T_1-weighted MRI to verify the feasibility of HMP-ICG&DOX as an in vivo MRI contrast agent. Model mice were anesthetized and injected with 100 μL of HMP-ICG&DOX suspension (20 mg/kg) via tail vein and imaged using a 3.0 T Philips MRI machine.

In vivo Photothermal Imaging

The SW1990 model mice were randomly divided into three groups, namely, PBS, HMP-ICG+Laser and HMP-ICG&DOX+Laser groups, in which PBS was the control group, and the drug (20 mg/kg) was administered by tail vein injection. After 4 h of drug administration, the model mice were anesthetized. The tumor site was irradiated (808 nm, 1 W/cm^2, 4 min), and the temperature change of the tumor site was recorded using an infrared thermography system.

In vivo Anti-Tumor Treatment Efficacy Assay

The 25 BALB/c model mice were divided into 5 groups of 5 mice each by random number table method, and were administered by tail vein injection at one day intervals, and the corresponding light treatments (808 nm, 1 W/cm^2, 4 min) were applied to the specific groups according to the experimental requirements, and the body weights of the model mice and the changes of the tumor volume were recorded at one day intervals at the same time. The experimental groups were PBS, Free DOX, HMP-DOX, HMP-ICG+Laser and HMP-ICG&DOX+Laser groups. At the end of the experimental cycle, the model mice were executed by cervical dislocation method, and the tumor tissue samples were collected, photographed and weighed. Blood samples were collected and serum samples were obtained by centrifugation for biochemical testing. Tumor tissues and major organs from nude mice in different treatment groups underwent H&E staining. Tumor tissues were further analyzed via TUNEL staining and CD8+ T cell immunohistochemical analysis to detect apoptosis and immune cell infiltration. Tumor volume formula:

$$\text{Tumor volume}\left(mm^3\right)=\frac{1}{2}\text{Length}\times\text{Width}^2$$

Statistical Analysis

The experiments were plotted and analyzed using GraphPad Prism 9.5 and Origin 2021 software. Continuous variables were expressed as mean±standard deviation, and for measurements that conformed to the normal distribution, one-way

ANOVA was used for comparisons between multiple groups, and paired t-tests were used for two-way comparisons between groups, and P<0.05 was considered to be statistically significant (ns: $P>0.05$, *$P<0.05$, **$P<0.01$, ***$P<0.001$, ****$P<0.0001$).

Result and Discussion

Preparation and Characterization of HMP-ICG&DOX NPs

Scheme 1 outlines the synthesis of HMP-ICG&DOX NPs. Firstly, monodisperse $sSiO_2$ NPs were synthesized by the hydrolysis reaction of TEOS. $sSiO_2$@MnO_2 NPs were then prepared by a redox reaction between $KMnO_4$ and $sSiO_2$ to form a layer of MnO_2 on the surface of well-dispersed $sSiO_2$. HM NPs were then prepared by dissolving the inner silica shells using Na_2CO_3 as an etching agent. To improve its water solubility and physiological stability, HMP NPs were obtained by modifying HM NPs with NH_2-PEG-NH_2. Finally, ICG and DOX were co-loaded into HMP NPs by electrostatic adsorption to obtain pH-responsive dual-modality imaging HMP-ICG&DOX NPs for subsequent experiments.

Transmission electron microscopy observation showed that $sSiO_2$ presented a relatively uniform solid spherical particle morphology with a smooth and well-dispersed surface, and its particle size was about 90 nm (Figure 1a). $sSiO_2$ @MnO_2 could be clearly seen that MnO_2 was uniformly wrapped around the surface of $sSiO_2$, forming a core-shell structure, and the thickness of MnO_2 was relatively uniform (Figure 1b). HM NPs were modified by Na_2CO_3 etching to

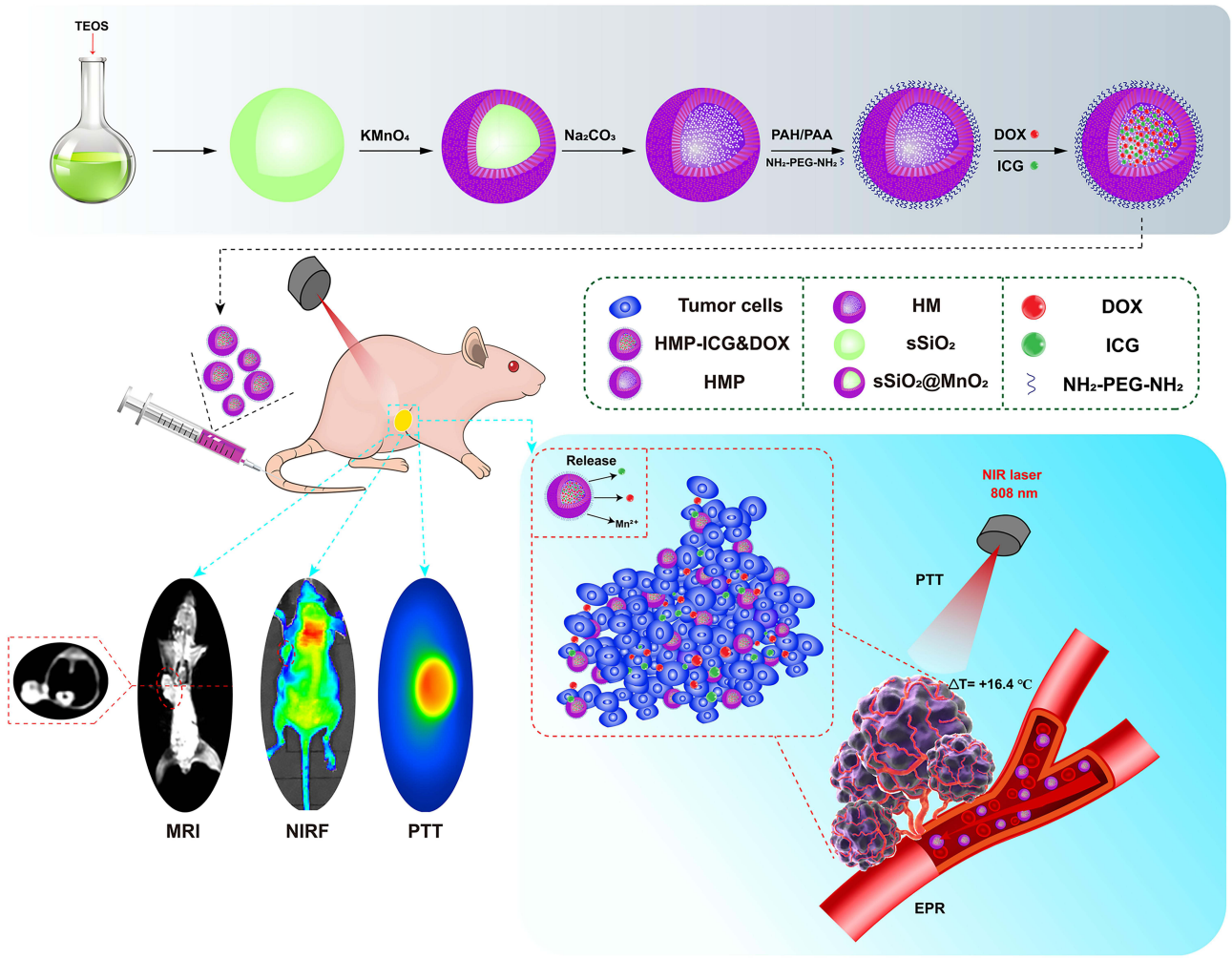

Scheme 1 Synthesis process and diagnosis and treatment mechanism of nanoparticles.

https://doi.org/10.2147/IJN.S542677

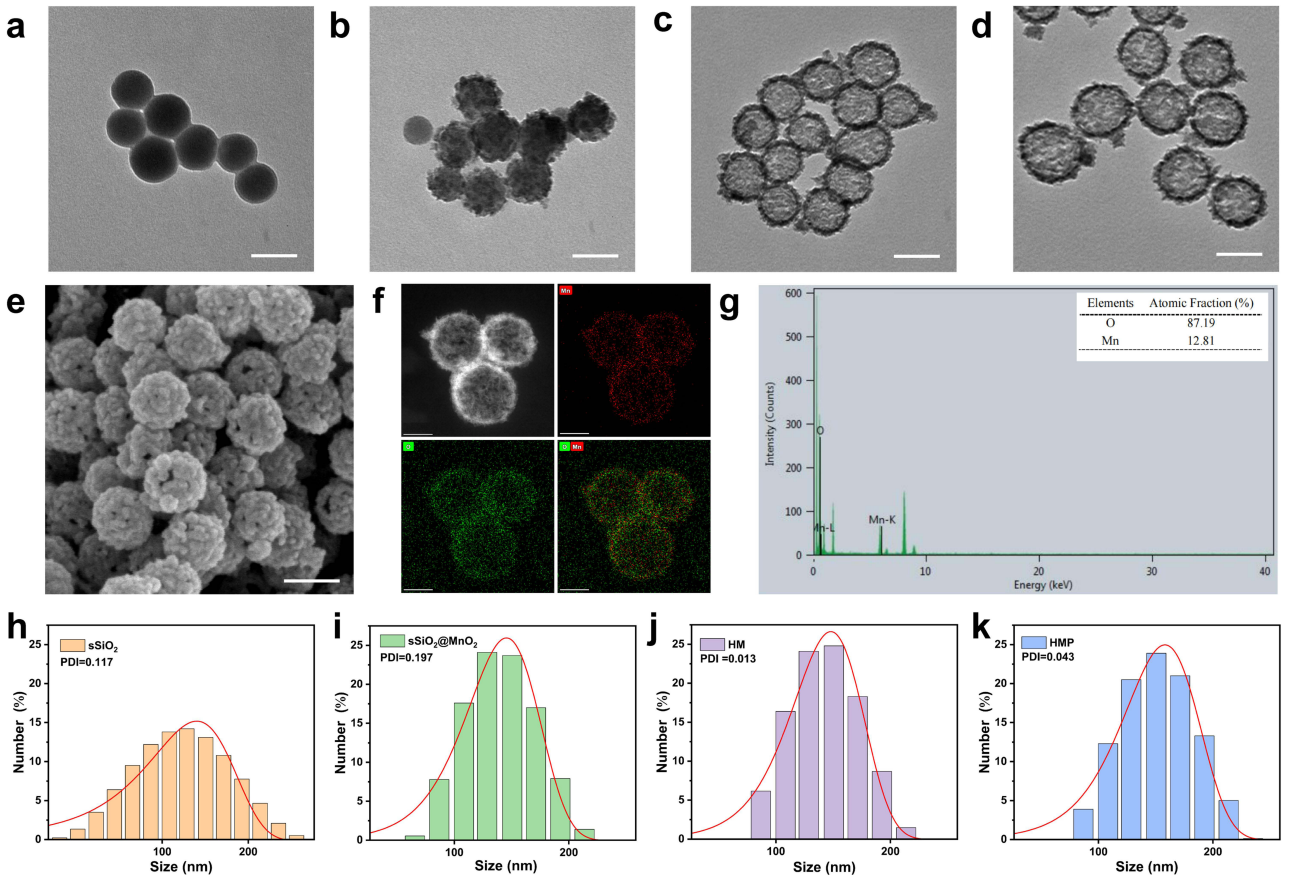

Figure 1 (**a–d**) TEM images of $sSiO_2$, $sSiO_2$@MnO_2, HM, and HMP NPs, respectively (scale bars: 100 μm); (**e**) SEM images of HMP NPs (scale bars: 100 μm); (**f**) High-resolution transmission electron microscopy and elemental mapping of HMP NPs (scale bars: 50 μm); (**g**) The energy dispersive spectra; (**h–k**) Hydrated particle size maps of $sSiO_2$, $sSiO_2$ @MnO_2, HM, and HMP NPs, respectively.

remove the internal $sSiO_2$ template, a hollow structure was formed, the thickness of the shell layer was uniform, and the internal cavity could be clearly seen (Figure 1c). The surface of the HMP NPs was slightly rough and well dispersed after NH_2-PEG-NH_2 modification, and the size and morphology of the particles were similar to those of the HM NPs, which indicated that there was not a significant change of the particle size in the process of NH_2-PEG-NH_2 modification (Figure 1d). The HMP NPs were shown by SEM to have a rough outer surface, which can be translated into a higher surface area, which is very favorable for drug delivery (Figure 1e). Elemental mapping images and corresponding X-ray energy spectra confirmed the presence of elements such as manganese and oxygen and their spatial distribution in HMP NPs (Figure 1f and g).

Dynamic light scattering showed that the hydrated particle size of the nanoparticles increased gradually after step-by-step modification, and the HMP NPs were slightly larger than the HM NPs, which was attributed to the successful modification of NH_2-PEG-NH_2 on the surface of the HM NPs (Figure 1h–k). It was shown that nanoparticles with a particle size of less than 200 nm were more favorable for enrichment at the tumor site through the EPR effect, which resulted in a more effective antitumor effect.[45] Surface potential test (Figure 2a) showed that the negative potential of the nanoparticles gradually weakened after modification, and the potential of HMP NPs changed from −25.6 mV to −12.37 mV, which further indicated that NH_2-PEG-NH_2 was successfully modified on the surface of HM NPs.

The total XPS spectra of HMP NPs showed the presence of elements such as O, Mn, and C (Figure 2b). Figure 2c shows the detailed spectrum of Mn element of HM nanoparticles. Analysis of the 2p orbital electrons of the binding energy of the Mn atoms in the nanoparticles shows that the Mn $2p_{3/2}$ peak is located near 641 eV and the Mn $2p_{1/2}$ peak is located near 653 eV, indicating that the element Mn exists mainly in the form of Mn^{4+} and that the element oxygen binds to Mn in the form of oxides to form the MnO_2 structure. The satellite peaks in the Mn 2p spectra appear near 644 eV,

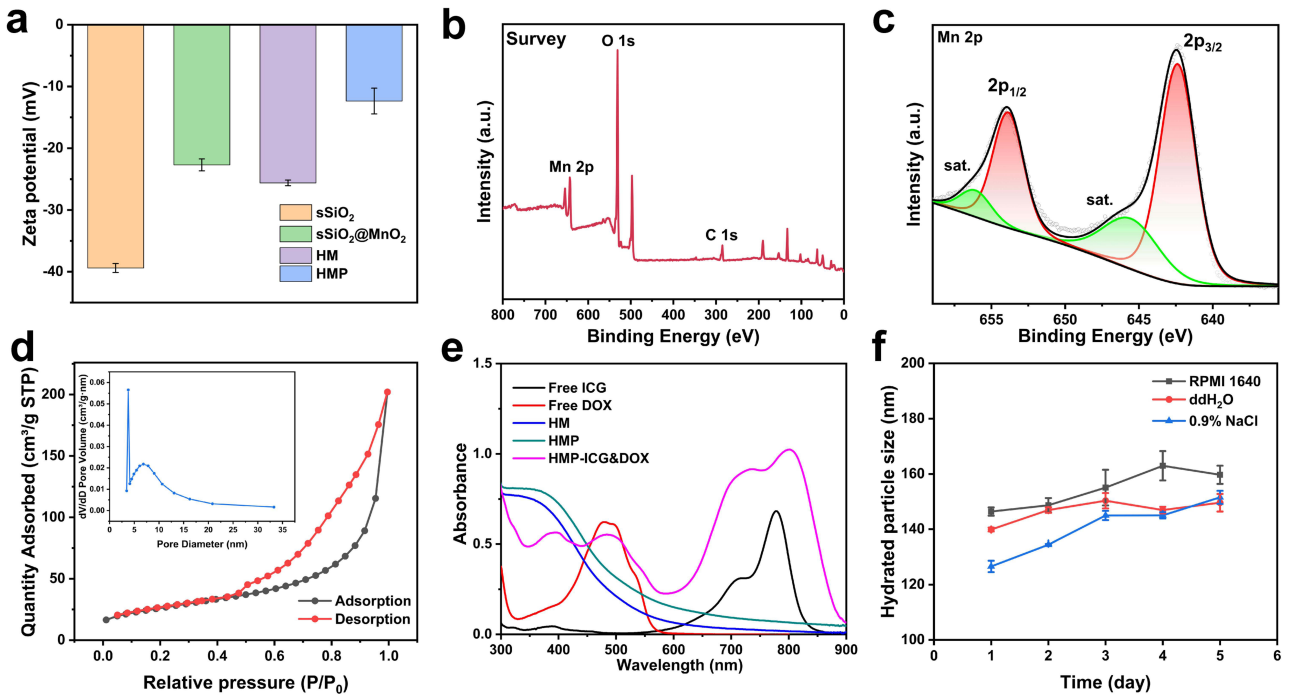

Figure 2 (**a**) Zeta potentials of $sSiO_2$, $sSiO_2$@MnO_2, HM and HMP; (**b** and **c**) XPS patterns of HM NPs; (**d**) Nitrogen adsorption and desorption profiles and pore size distributions of HMP NPs; (**e**) Ultraviolet absorption spectra of the nanoparticles; (**f**) Particle size changes of HMP in different solvents.

further proving that the element manganese is present in the form of Mn^{4+}. Figure S1 shows the XRD pattern of HMP NPs, which shows characteristic diffraction peaks near 2θ=37.3° and 66.3°, and the diffraction peaks are overall broader, indicating that HMP NPs exist in an amorphous state.

The surface area of the hollow material is crucial for drug encapsulation and controlled release. As shown in Figure 2d, the specific surface area of HMP was calculated using the BET method to be 93.03 m^2/g, with an average pore size of 8.99 nm. In the region of low relative pressure ($P/P_0 < 0.1$), the amount of adsorption increased gradually with the rise in relative pressure. As relative pressure continued to increase, the adsorption amount rose sharply, particularly as it approached 1.0, where the maximum adsorption value was reached. This observation indicates a large specific surface area and an abundant pore structure. The adsorption and desorption curves did not completely overlap, forming a distinct H3-type hysteresis loop, which is characteristic of a typical IV-type isotherm. These data demonstrate that the hollow porous structure of HMP, with its large specific surface area, serves as an ideal drug carrier.

As shown in Figure 2e, the absorption spectra of HMP NPs and HM NPs were similar, indicating that the modification of NH_2-PEG-NH_2 does not affect the UV absorption properties of HM NPs. The absorption peaks of ICG and DOX were visible in the UV spectra of the HMP-ICG&DOX solution, which can indicate that ICG and DOX were successfully loaded into HMP to form dual-drug co-loaded nanoparticles for synergistic therapy. In particular, the absorption peaks of ICG in HMP-ICG&DOX were red-shifted, probably due to the conversion of ICG monomers to J aggregates through non-chemical bonding.[46] In addition Raman spectra showed a characteristic peak of MnO_2 at 574 cm^{-1}, indicating that HM NPs were successfully prepared (Figure S2).

Stability of Nanoparticles

The stability of nanoparticles is critical in drug delivery applications.[10] HMP NPs remained stable particle size and free of aggregation precipitation after 5 days of placement in a variety of media (RPMI 1640, deionized water, saline) (Figure 2f).

https://doi.org/10.2147/IJN.S542677

Encapsulation Rate, Drug Loading and in vitro Drug Release Assay of HMP-ICG&DOX NPs

The absorption peaks of ICG and DOX were identified at wavelengths of 780 nm and 480 nm, respectively. The equations for the standard curves were determined as y=0.1598x+0.0417 (R^2=0.999) and y=0.0193x+0.0042 (R^2=0.999), demonstrating strong linearity, as illustrated in Figure S3. The drug encapsulation of HMP-ICG&DOX NPs was calculated using the above standard curves, and the results were shown in Figure 3a and b. The drug loading of ICG in HMP-ICG&DOX NPs was 12.16%, with an encapsulation rate of 85.15%, and that of DOX was 11.27%, with a 78.86% encapsulation rate.

Manganese dioxide has been shown to be stable under neutral pH conditions but degrades under acidic conditions.[47,48] Therefore, HMP NPs were incubated at three different pH conditions (7.4, 6.8 and 5.5) and samples were removed at specific time points for observation by TEM (Figure 3c). After 8 h of incubation in a neutral environment, no significant changes in the morphology of HMP NPs were observed. However, under acidic conditions, the HMP NPs showed obvious time-dependent degradation behavior. Then the drug release performance of HMP-ICG&DOX NPs was evaluated at different pH values. As shown in Figure 3d and e, the release efficiency of ICG and DOX is very slow at pH=7.4. In contrast, the drug release rate significantly increased at pH=6.8 or pH=5.5. Specifically, at pH 5.5, the release rates of ICG and DOX reached 42.49% and 71.41% respectively within 24 h. At pH 6.8, the release rates were 27.7% and 36.73%, whereas at pH 7.4, the release rates were only 18.12% and 24.14%. Drug release reached equilibrium after 24 h. This demonstrates that HMP-ICG&DOX NPs exhibit pH sensitivity, enabling regulation of drug release rates in response to environmental pH changes.

In vitro Photothermal Performance Results

To evaluate the photothermal performance of HMP-ICG&DOX, experiments were conducted to compare the warming of ddH_2O, Free DOX, Free ICG, HMP, and HMP-ICG&DOX NPs under the irradiation of an 808 nm laser (1.0 W/cm^2) (Figure 3f). The results indicated that HMP-ICG&DOX NPs exhibited a significant photothermal effect, outperforming Free ICG in this regard. Further studies revealed a concentration-dependent photothermal performance of HMP-ICG&DOX NPs; specifically, the aqueous solution temperature increased to only 8 °C at a concentration of 12.5 μg/mL, whereas it rose to 29.95 °C at a concentration of 125 μg/mL (Figure 3g). Additionally, we investigated the relationship between temperature rise and laser power, observing an increase of only 9.75 °C at a power density of 0.5 W/cm^2, while the aqueous solution temperature rose by 31.26 °C at a power density of 1.5 W/cm^2 (Figure 3h). We further investigated the photothermal stability of HMP-ICG&DOX NPs and Free ICG. After five freeze-thaw cycles, the maximum temperature of HMP-ICG&DOX NPs decreased from 21.87 °C to 16.26 °C, while that of the Free ICG group decreased from 13.35 °C to 4.5 °C. This demonstrates the excellent photothermal stability of HMP-ICG&DOX NPs (Figures 3i and S4). The photothermal conversion efficiency of HMP-ICG&DOX NPs reached 32.25%, whereas that of Free ICG was only 14.6% (Figures S5 and S6). Furthermore, an infrared thermal imager was utilized to obtain photothermal images of the solutions at varying concentrations, revealing that the color of the solutions transitioned from light yellow to light red as the concentration and irradiation time increased (Figure 3j).

Magnetic Resonance Imaging Results

HMP-ICG&DOX NPs gradually brightened with the increase of Mn^{2+} concentration under acidic conditions (pH=5.5), and the relaxation rate was calculated with r_1=6.0311 $mM^{-1}\cdot s^{-1}$. In contrast, the nanoparticles did not change due to the increase of the Mn^{2+} concentration under neutral conditions, and the calculated period relaxation rate was only 0.6173 $mM^{-1}\cdot s^{-1}$. The results indicate that HMP-ICG&DOX is relatively stable under neutral conditions, but degrades to produce Mn^{2+} under acidic conditions, resulting in T_1 imaging (Figure 3k and l).

Biocompatibility

Safety and non-toxicity are prerequisites for the application of drug delivery systems. By incubating HMP NPs at different concentrations (6.25–200 μg/mL) with HPDE6C7 and SW1990 cells for 24 h, it was found that the survival rate of both types of cells was more than 85% even at 200 μg/mL (Figure 4a). As shown in Figure 4b, the hemolysis rate of all experimental groups was less than 5%, which met the criteria for hemolysis of biomaterials. In the in vivo

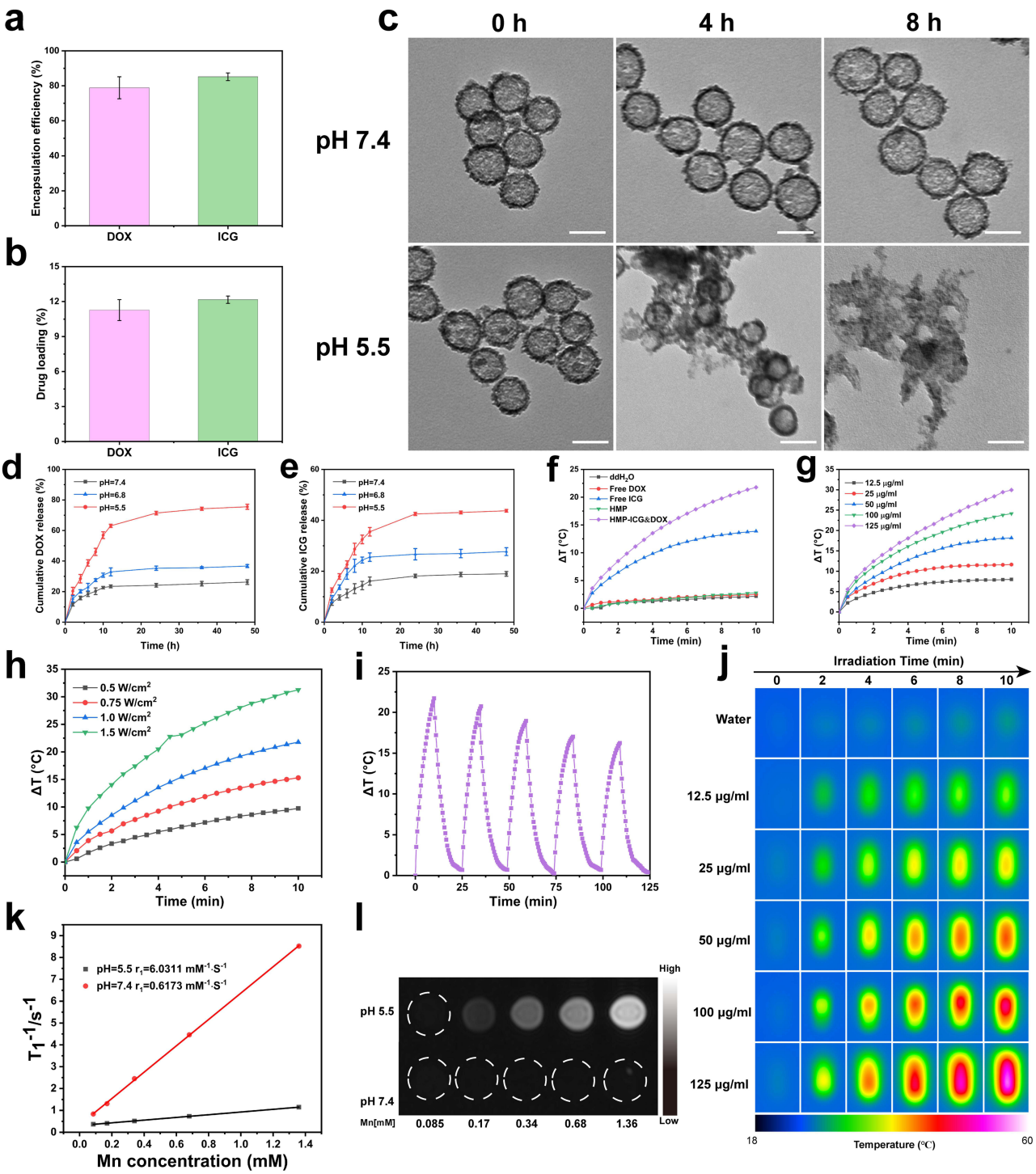

Figure 3 (**a** and **b**) Encapsulation rate and drug loading of DOX and ICG in HMP-ICG&DOX NPs; (**c**) Transmission electron microscopy images of nanoparticles under different pH conditions (scale bars: 100 μm) (**d** and **e**) In vitro release profiles of DOX and ICG from HMP-ICG&DOX at different pH; (**f**) Warming of nanoparticles under 808 nm laser irradiation for 10 min; (**g**) Warming of HMP-ICG&DOX NPs with different concentrations of 808 nm laser irradiation within 10 min; (**h**) Warming of HMP-ICG&DOX NPs with different power densities under 808 nm laser irradiation within 10 min; (**i**) Temperature changes of HMP-ICG&DOX NPs in 5 hot and cold cycling cycles; (**j**) Photothermal images of HMP-ICG&DOX NPs at different concentrations under 808 nm laser irradiation; (**k**) Relaxation rate of HMP-ICG&DOX NPs at different pH values; (**l**) T_1-weighted MR maps of HMP-ICG&DOX at different pH values (the dotted circle indicates the position of the centrifuge tube).

https://doi.org/10.2147/IJN.S542677

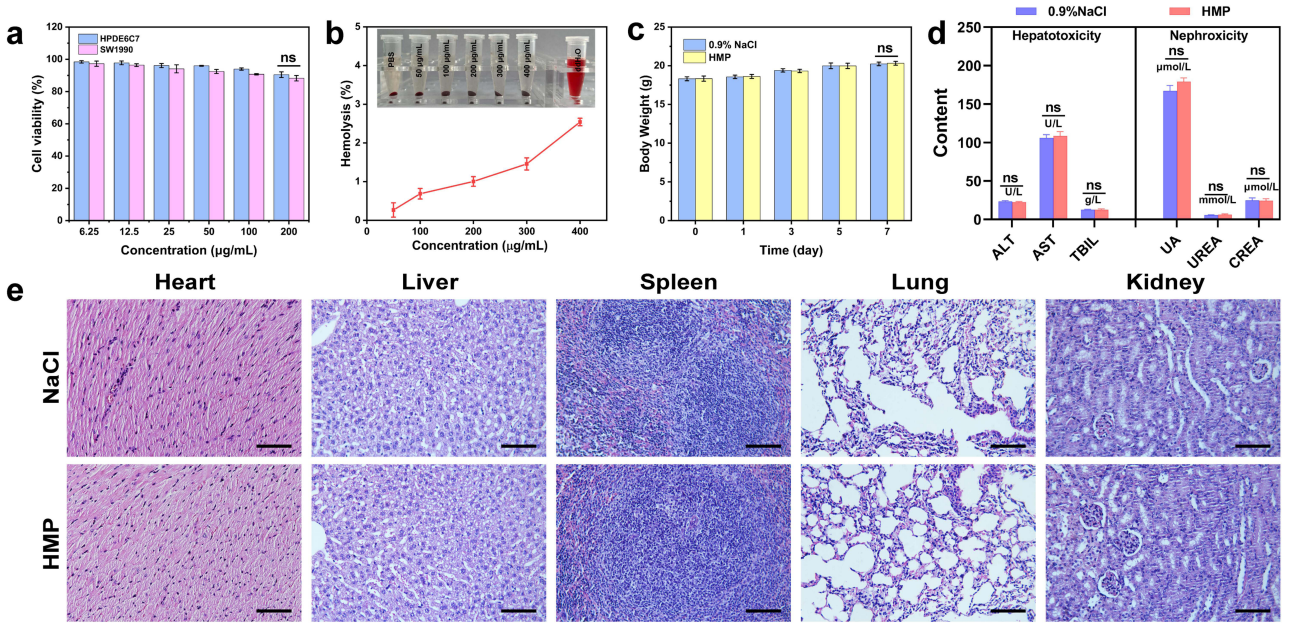

Figure 4 (**a**) Cell survival of HPDE6C7 and SW1990 cells after incubation with different concentrations of HMP nanoparticles for 24 h; (**b**) Hemolysis of erythrocytes by HMP NPs; (**c**) Changes in body weight of nude mice within one week; (**d**) Biochemical indices of liver and kidney functions; (**e**) H&E stained images of nude mice (scale bars: 100 μm, ns: $P>0.05$).

experiments, we monitored the body weights of the nude mice in the HMP group and the saline group, and Figure 4c shows that there was no weight loss or death in the nude mice in the HMP group. In addition, serum biochemical indexes (ALT, AST, TBIL, UA, UREA, CREA) of nude mice in the saline group and HMP group were examined to further determine whether the HMP NPs influenced the normal function of the organism. As can be seen from the results of Figure 4d and e, the blood biochemical indexes of liver and kidney functions and H&E staining results showed that the major organs of nude mice in the HMP group were not significantly damaged. The above results indicate that HMP NPs are highly biocompatible.

In vitro Cellular Uptake Assay

Effective tumor visualization and treatment largely depend on whether nanomaterials can be efficiently internalized by cells. Laser confocal microscopy revealed that tumor cells treated with HMP-ICG&DOX NPs exhibited significantly enhanced red fluorescence intensity compared to the Free DOX group, while the PBS group showed only blue fluorescence (DAPI) (Figure 5a). This indicated that the nanoparticles were able to enter the cells effectively and could achieve effective accumulation in the tumor cells. Then the results of HMP-ICG&DOX NPs were observed after co-incubation with SW1990 cells for 0 h 1 h, 2 h, and 4 h (Figure 5b), and the fluorescence intensity of the cells was enhanced with the increase of incubation time. To further investigate the uptake of HMP-ICG&DOX in SW1990 cells, quantitative fluorescence analysis was performed using flow cytometry. As shown in Figure 5c, the fluorescence intensity of HMP-ICG&DOX was enhanced with increasing incubation time. Multiple results demonstrated that HMP-ICG&DOX NPs were efficiently uptaken into tumor cells.

Cytotoxicity Assay

As shown in Figure 5d and e, with the increase of drug concentration, the inhibitory effect of each group on HPDE6C7 and SW1990 cells was improved to varying degrees. At the highest drug concentration in the experimental range, the survival rates of the two types of cells were 66% and 68% in the Free DOX group, 64% and 61% in the HMP-DOX group, 46% and 47% in the HMP-ICG+Laser group, and the lowest in the HMP-ICG&DOX+Laser group, 37% and 33%, respectively. At the highest drug concentration within the experimental range, the CI for the HMP-ICG&DOX NPs+Laser group was 0.6, demonstrating

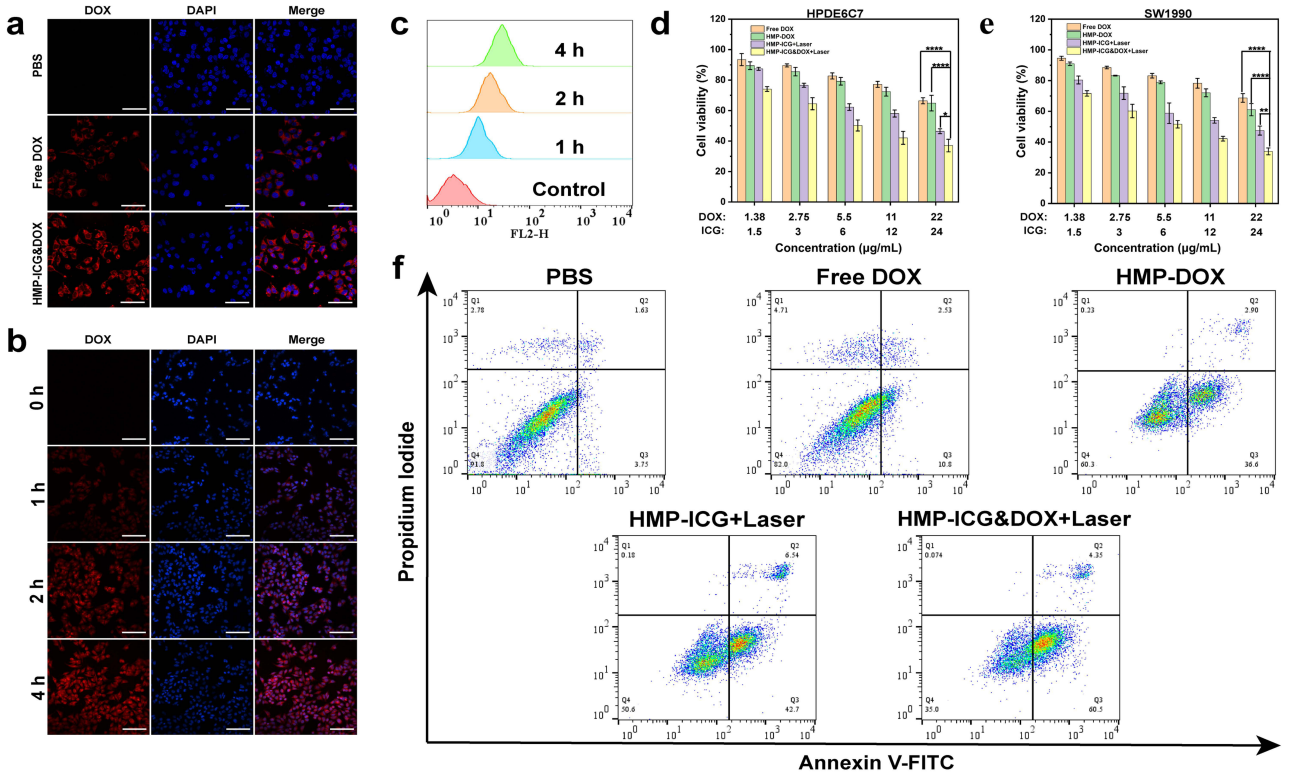

Figure 5 (**a**) CLSM images of Free DOX and HMP-ICG&DOX after incubation with SW1990 cells; (**b**) CLSM images of HMP-ICG&DOX incubated with SW1990 cells at different time points; (**c**) Relative fluorescence intensity flow cytometry images of SW1990 cells; (**d** and **e**) HPDE6C7 and SW1990 cells incubated with cell survival after incubation with different concentrations of each group of nanoparticles; (**f**) Apoptosis plots for different nanoparticles (scale bars: 50 μm, ****P<0.0001, **P<0.01, *P<0.05).

synergistic effects. The experimental results provide compelling evidence that combination therapy demonstrates markedly superior efficacy in inhibiting tumour cell growth compared to monotherapy. The introduction of the nano drug-carrying system enables the drug to be stably dispersed in the aqueous solution and easily taken up by the cells, which effectively enhances the bioavailability of the drug molecules and thus significantly enhances the inhibitory effect on tumor cells.

Apoptosis Assay

The apoptosis of SW1990 cells after different treatments was detected by flow cytometry and Annexin V-FITC detection kit (Figure 5f). The results showed that the apoptosis rates were 5.38%, 13.33%, 39.5%, 49.24%, and 64.85% in the PBS group, FreeDOX group, HMP-DOX group, HMP-ICG+Laser group, and HMP-ICG&DOX+Laser group, respectively. Consistent with the results of CCK-8 experiment, the apoptosis rate of HMP-ICG&DOX+Laser group was significantly higher than that of other groups due to the combination of chemotherapy and PTT. The experimental results indicated that the combined treatment of chemotherapy and PTT could significantly enhance the ability of HMP-ICG&DOX to induce apoptosis. This is because, on the one hand, the temperature increase induced by PTT promoted the uptake of nanoparticles in tumor cells and accelerated the release of DOX; on the other hand, DOX acted on the tumor cells to improve their sensitivity to the temperature increase, which further enhanced the effect of PTT treatment.

In vivo Fluorescence Imaging

As illustrated in Figure 6a, the fluorescence signals of HMP-ICG&DOX NPs exhibited a time-dependent pattern over the detection period of 0–24 h, peaking at 4 h. The fluorescence intensity of HMP-ICG&DOX NPs consistently surpassed that of the free ICG group across all time points. Notably, at each time point, the fluorescence intensity at the tumor site in model mice treated with HMP-ICG&DOX was significantly higher than that in the free ICG group. This difference can be attributed to the inherent instability and self-aggregating nature of ICG in physiological environments, which leads to its rapid clearance from

https://doi.org/10.2147/IJN.S542677

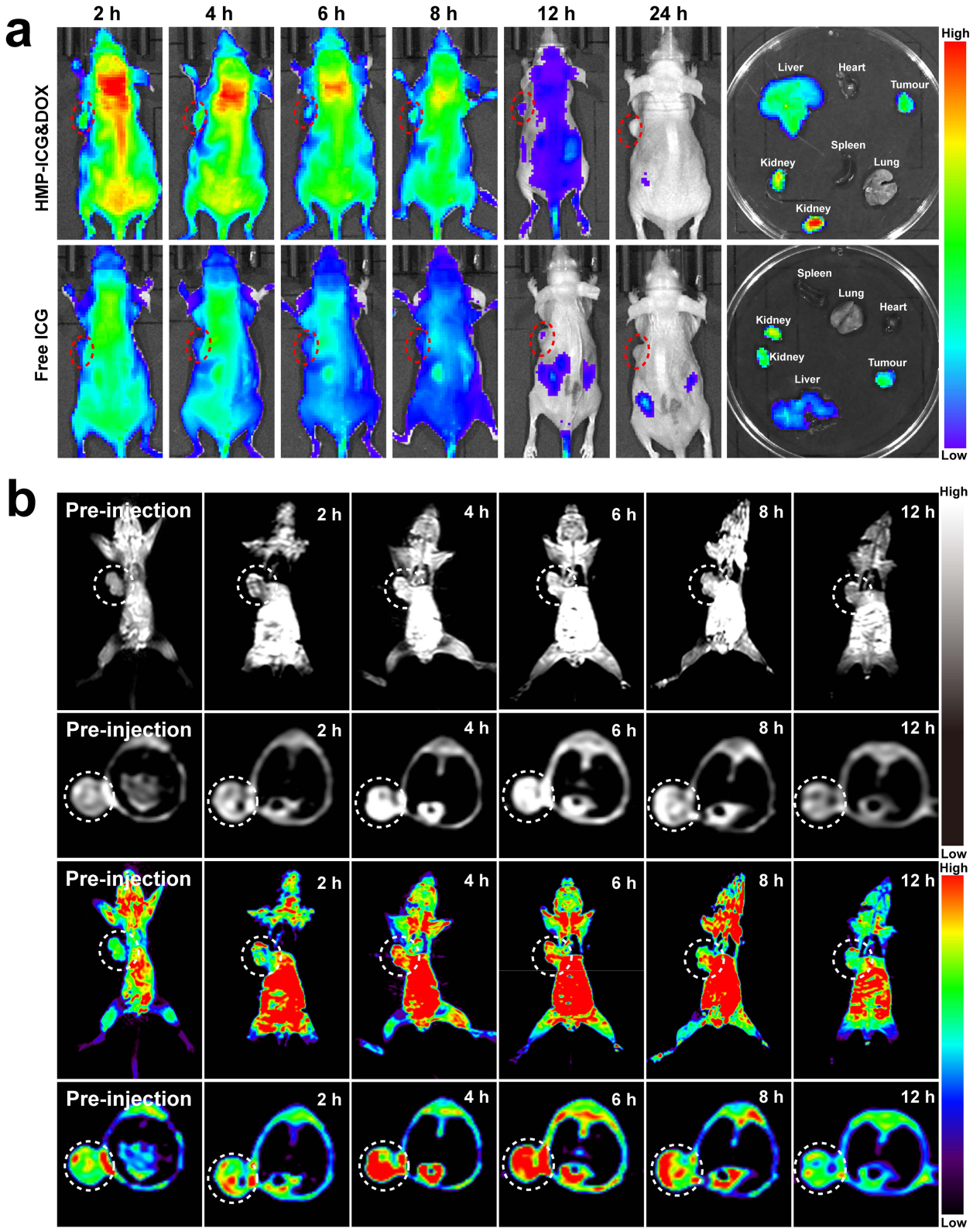

Figure 6 (**a**) Near-infrared fluorescence imaging and imaging of major organs and tumor tissues in model rats after tail vein injection of HMP-ICG&DOX NPs and free ICG; (**b**) T_1 magnetic resonance imaging of model rats at different time points after injection of HMP-ICG&DOX NPs (the dashed circle indicates the location of the tumor).

the body. In contrast, the enhanced fluorescence intensity observed at the tumor site for HMP-ICG&DOX NPs can be explained by the enhanced permeability and retention (EPR) effect. EPR facilitates prolonged retention of ICG within the tumor and enhances its accumulation, as the incorporation of HMP NPs reduces the degradation rate of ICG. After 24 h post-administration, the model mice were euthanised and major organs and tumour tissues were retrieved for in vitro imaging. The HMP-ICG&DOX NPs group exhibited strong near-infrared fluorescence signals in tumour tissues, liver, and kidneys. This result visually demonstrated significant nanoparticle accumulation in both liver and tumour tissues, with clearance primarily via renal excretion. Compared to the HMP-ICG&DOX NPs group, the Free ICG group exhibited comparatively weaker fluorescence signals in tumour tissues. This further demonstrates that the nanocarrier effectively enhances ICG accumulation at tumour sites and prolongs drug retention time. Additionally, Mn^{2+} levels in major organs were determined using inductively coupled plasma mass spectrometry (ICP-MS). Elemental Mn accumulated mainly in the liver and kidney 24 h after administration (Figure S7). These findings indicate that HMP-ICG&DOX NPs degrade in vivo and are metabolized by the liver and kidneys, ensuring their biosafety.

In vivo Magnetic Resonance Imaging

The manganese dioxide in the nanoparticles degrades responsively in the tumor environment to generate Mn^{2+}, which is considered as a T_1 contrast agent for magnetic resonance imaging due to its occupation of five unpaired 3d electrons.[49] Figures 6b and S8 depict the in vivo magnetic resonance imaging of HMP-ICG&DOX nanoparticles and the time-dependent signal intensity curves within tumor tissue. Following tail vein injection of HMP-ICG&DOX into model mice, the T_1 signal at the tumor site increased over time, peaking at 4 h before gradually diminishing. This further indicates that nanoparticles effectively accumulate at the tumor site and release Mn^{2+}, demonstrating potential as an effective T_1 contrast agent.

In vivo Photothermal Imaging

Leveraging the photothermal conversion capabilities of HMP-ICG&DOX, we conducted in vivo monitoring of the tumor-targeting enrichment and photothermal performance of the nanoparticles through NIR imaging. As shown in Figure S9, the model mice in the PBS group showed no obvious temperature change, and the degree of temperature increase in the HMP-ICG&DOX+Laser group was higher than that in the HMP-ICG+Laser group at different time points, and the highest temperature in 4 min could reach 47.94 °C, which had a good photothermal effect, confirming that the HMP-ICG&DOX+Laser group, at the level of animal experiments The HMP-ICG&DOX+Laser group has the experimental basis for realizing photothermal therapy at the animal experiment level.

In vivo Anti-Tumor Therapy Outcomes

The antitumour efficacy of HMP-ICG&DOX NPs was evaluated in SW1990 model mice via tail vein injection every other day, followed by 4 min of laser irradiation to the tumour region 4 h post-administration. (Figure 7a). Compared to other experimental groups, the tumor volume in the HMP-ICG&DOX+Laser group was significantly reduced after treatment, demonstrating a decrease from the initial volume and effectively inhibiting tumor tissue growth, thereby achieving a notable anti-tumor effect (Figure 7b). At the conclusion of the treatment, the model mice were euthanized, and tumor tissues were collected for imaging and weighing (Figure 7c and d), with results consistent with in vivo observations. Furthermore, as illustrated in Figure 7e, there were no significant changes in the body weight of the model mice throughout the experiment, indicating that HMP-ICG&DOX+Laser exhibited no apparent toxic side effects and maintained high biosafety. Blood biochemical analyses revealed no significant differences in liver and kidney function indices between the HMP-ICG&DOX NPs and the PBS group (Figure 7f). Subsequently, H&E staining results of tumor tissues across all experimental groups were further analyzed (Figure 7g). The HMP-ICG&DOX+Laser group exhibited pronounced nuclear fragmentation and nucleolysis, a reduction in necrotic cell disintegration, and the lowest cell count, indicating that a majority of the cells had undergone death. Tunel analysis confirmed that apoptosis was most prominent in the HMP-ICG&DOX+Laser group, aligning with the H&E findings. CD8+ T cells, as pivotal cytotoxic T lymphocytes, possess the capacity to directly recognise and eliminate tumor cells, serving as core effector cells in antitumor immunity.[50,51] Immunohistochemical analysis of tumor tissue revealed that the HMP-ICG&DOX+Laser group exhibited the highest density of CD8+ T cells within the tumor region compared to other treatment groups. This finding

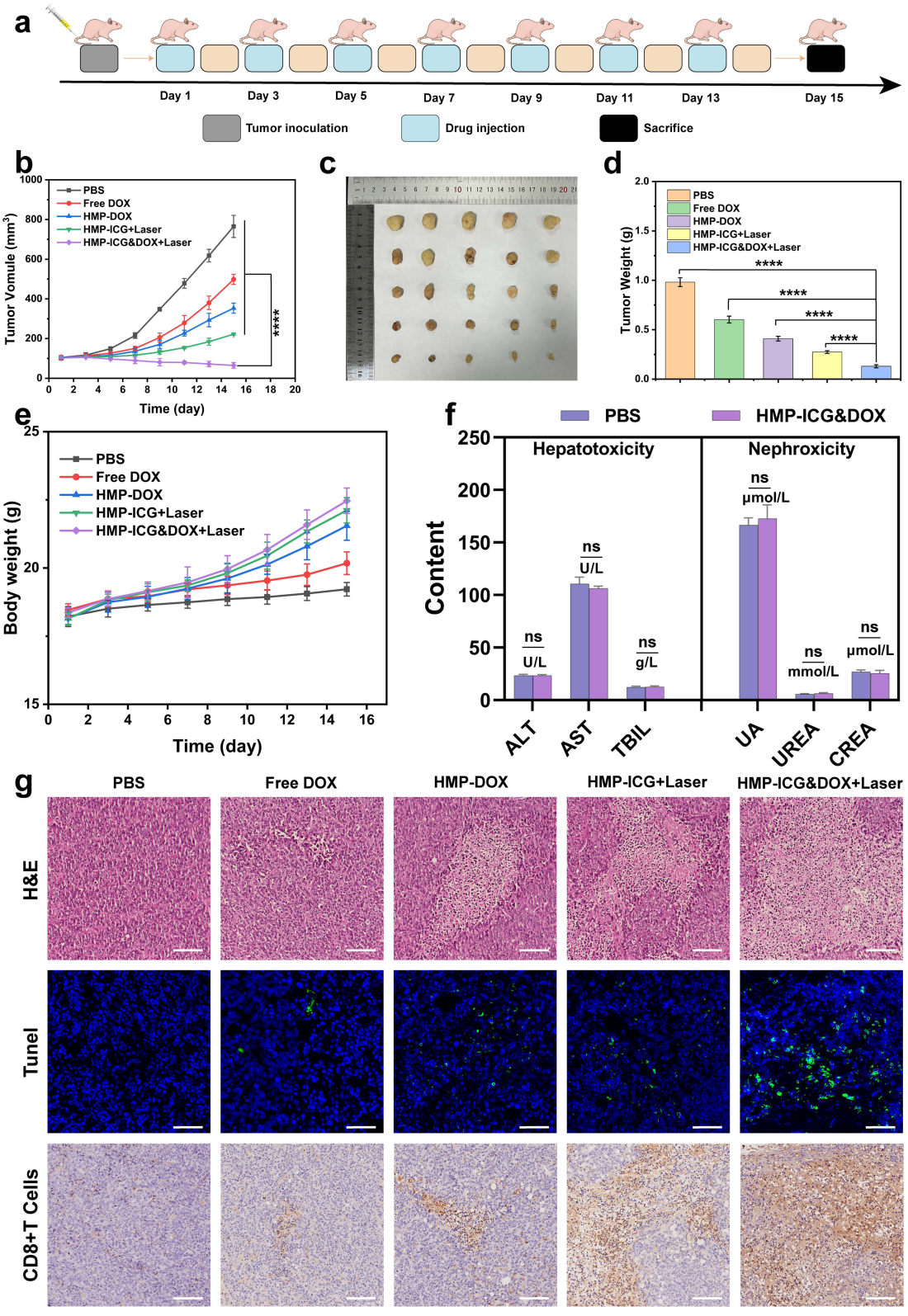

Figure 7 (**a**) Schematic diagram of pancreatic cancer model mice treated with HMP-ICG&DOX; (**b**) Changes in tumor volume of model mice in each group; (**c**) Appearance of tumor tissues of model mice in each group; (**d**) Comparison of tumor weight of model mice in each group; (**e**) Changes in body weight of model mice in each group; (**f**) Blood biochemical indices of model mice; (**g**) H&E (scale bar: 100μm), Tunel (scale bar: 50 μm) and CD8+ T cells (scale bar: 100μm) staining of model mice tumor tissues in different treatment groups (****P<0.0001, ns: P>0.05).

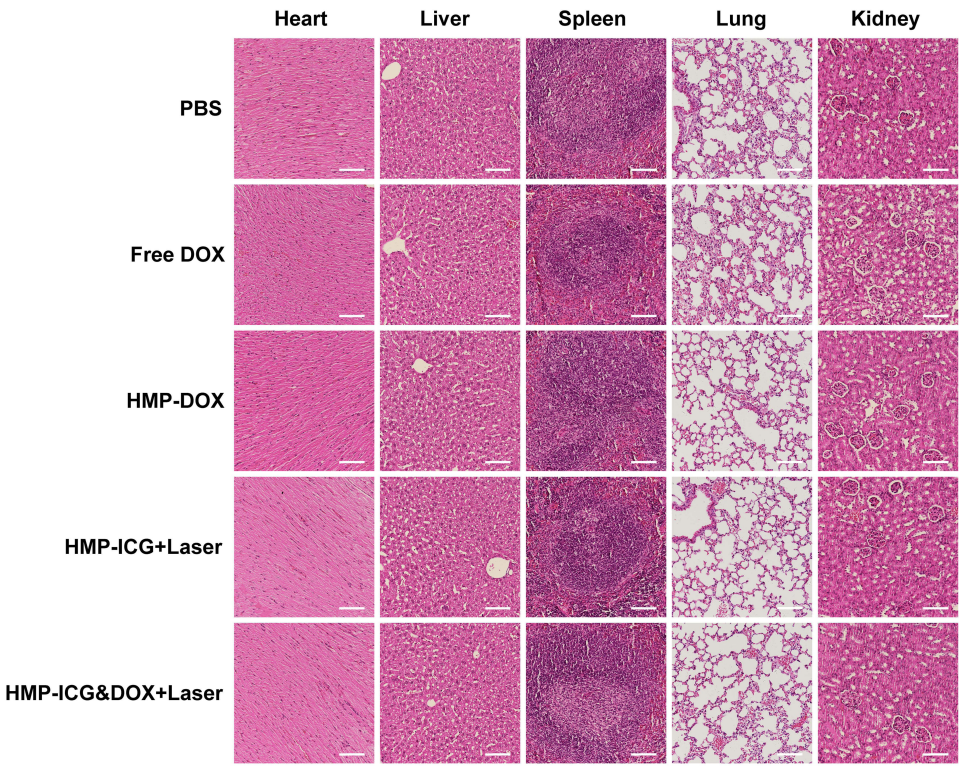

Figure 8 H&E staining of major organs of model mice in different treatment groups (scale bar: 100 μm).

indicates that this therapeutic approach significantly promotes the infiltration of cytotoxic T cells into tumor tissue. The experimental results at the histological level were consistent with those observed at the cellular and organ levels, thereby confirming the significant anti-tumor effects of HMP-ICG&DOX NPs.

As shown in Figure 8, after histopathological analysis, the H&E staining of major organs in each group showed that there was no obvious abnormality in the tissue structure, and the cell structure was normal. This indicates that HMP-ICG&DOX NPs have no obvious toxic side effects, are biologically safe, and do not have serious effects on major organs in the body when they have antitumor efficacy.

Conclusions

In this study, a novel pH-responsive multifunctional nanoprobe, HMP-ICG&DOX, was developed and combined with the dual modality of photothermal therapy and chemotherapy, which successfully improved the therapeutic effect of pancreatic cancer without any obvious toxic side effects. The HMP-ICG&DOX nanoparticles also possessed the multimodal imaging ability, which enabled real-time monitoring of tumors during the tumor treatment process. Finally, in vivo and in vitro experiments have demonstrated that HMP-ICG&DOX can inhibit the growth of pancreatic cancer cells more effectively and have good biological safety. Therefore, HMP-ICG&DOX has a wide range of application prospects in tumor diagnosis and treatment and provides a new strategy for the integration of pancreatic cancer diagnosis and treatment.

Data Sharing Statement

The data and materials in the current study are available from the first author Na Li upon reasonable request.

Ethics Approval

This study was conducted in accordance with the experimental procedures established by the Animal Ethics Research Center of Qiqihar Medical University (QMU-AECC-2024-152). In adherence to the ARRIVE guidelines, we ensured compliance with the "Regulations on the Management of Experimental Animals of the People's Republic of China" and other relevant

regulations concerning animal experimentation. Our methodology emphasizes the significance of the welfare of the experimental animals and aims to minimize any adverse impacts on their well-being throughout the research process.

Acknowledgments

This work was supported by the Heilongjiang Provincial Health and Wellness Commission Fund Project (20240909010090) and Construction Project of Dominant Characteristic Disciplines of Qiqihar Medical University (QYZDXK-009).

Disclosure

The authors report no conflicts of interest in this work.

References

1. Siegel RL, Giaquinto AN, Jemal A. Cancer statistics, 2024. *CA Cancer J Clin*. 2024;74(1):12–49. doi:10.3322/caac.21820
2. Zhang H, Cao K, Xiang J, Zhang M, Zhu M, Xi Q. Hypoxia induces immunosuppression, metastasis and drug resistance in pancreatic cancers. *Cancer Lett*. 2023;571:216345. doi:10.1016/j.canlet.2023.216345
3. Cahoon AR, Smith BD, Yang WT. Internal thoracic lymphadenopathy in breast cancer. *Radiographics*. 2017;37(4):1024–1036. doi:10.1148/rg.2017160166
4. Tempero MA, Malafa MP, Al-Hawary M, et al. Pancreatic adenocarcinoma, version 2.2021, NCCN clinical practice guidelines in oncology. *J Natl Compr Canc Netw*. 2021;19(4):439–457. doi:10.6004/jnccn.2021.0017
5. Chintamaneni PK, Pindiprolu S, Swain SS, et al. Conquering chemoresistance in pancreatic cancer: exploring novel drug therapies and delivery approaches amidst desmoplasia and hypoxia. *Cancer Lett*. 2024;588:216782. doi:10.1016/j.canlet.2024.216782
6. Eyck BM, Onstenk BD, Noordman BJ, et al. Accuracy of detecting residual disease after neoadjuvant chemoradiotherapy for esophageal cancer: a systematic review and meta-analysis. *Ann Surg*. 2020;271(2):245–256. doi:10.1097/sla.0000000000003397
7. Shah VM, Sheppard BC, Sears RC, Alani AW. Hypoxia: Friend or Foe for drug delivery in pancreatic cancer. *Cancer Lett*. 2020;492:63–70. doi:10.1016/j.canlet.2020.07.041
8. Springfeld C, Ferrone CR, Katz MHG, et al. Neoadjuvant therapy for pancreatic cancer. *Nat Rev Clin Oncol*. 2023;20(5):318–337. doi:10.1038/s41571-023-00746-1
9. Huang A, Li Q, Shi X, et al. An iron-containing nanomedicine for inducing deep tumor penetration and synergistic ferroptosis in enhanced pancreatic cancer therapy. *Mater Today Bio*. 2024;27:101132. doi:10.1016/j.mtbio.2024.101132
10. Shi G, Li Z, Li N, et al. Gelatin-coated glutathione depletion and oxygen generators in potentiated chemotherapy for pancreatic cancer. *Int J Biol Macromol*. 2024;280:135973. doi:10.1016/j.ijbiomac.2024.135973
11. Krissanaprasit A, Key CM, Pontula S, LaBean TH. Self-assembling nucleic acid nanostructures functionalized with aptamers. *Chem Rev*. 2021;121(22):13797–13868. doi:10.1021/acs.chemrev.0c01332
12. Yang J, Zhu J, Lu S, Qin H, Zhou W. Transdermal psoriasis treatment inspired by tumor microenvironment-mediated immunomodulation and advanced by exosomal engineering. *J Control Release*. 2025;382:113664. doi:10.1016/j.jconrel.2025.113664
13. Yuan H, Chen Y, Hu Y, et al. Disulfide bond-driven nanoassembly of lipophilic epirubicin prodrugs for breast cancer therapy. *J Pharm Investig*. 2025:1–4. doi:10.1007/s40005-025-00731-z
14. Tong F, Wang Y, Gao H. Progress and challenges in the translation of cancer nanomedicines. *Curr Opin Biotechnol*. 2024;85:103045. doi:10.1016/j.copbio.2023.103045
15. Ma R, Alifu N, Du Z, et al. Indocyanine green-based theranostic nanoplatform for NIR fluorescence image-guided chemo/photothermal therapy of cervical cancer. *Int J Nanomed*. 2021;16:4847–4861. doi:10.2147/ijn.s318678
16. Fang H, Chu SA, Xia Y, Wang KW. Programmable self-locking origami mechanical metamaterials. *Adv Mater*. 2018;30(15):e1706311. doi:10.1002/adma.201706311
17. Xiao T, He M, Xu F, et al. Macrophage membrane-camouflaged responsive polymer nanogels enable magnetic resonance imaging-guided chemotherapy/chemodynamic therapy of orthotopic glioma. *ACS Nano*. 2021;15(12):20377–20390. doi:10.1021/acsnano.1c08689
18. Guan S, Liu X, Li C, et al. Intracellular mutual amplification of oxidative stress and inhibition multidrug resistance for enhanced sonodynamic/chemodynamic/chemo therapy. *Small*. 2022;18(13):e2107160. doi:10.1002/smll.202107160
19. Jiang Y, Li Y, Wang K, Feng X, Han L, Yang H. MnO2-based bioresponsive nanoplatform synergizing mitochondrial metabolism modulation for amplified phototherapy and chemodynamic therapy of melanoma. *Chem Eng J*. 2025;504:158757. doi:10.1016/j.cej.2024.158757
20. Yang G, Xu L, Chao Y, et al. Hollow MnO_2 as a tumor-microenvironment-responsive biodegradable nano-platform for combination therapy favoring antitumor immune responses. *Nat Commun*. 2017;8(1):902. doi:10.1038/s41467-017-01050-0
21. Wang Y, Xu Y, Song J, et al. Tumor cell-targeting and tumor microenvironment-responsive nanoplatforms for the multimodal imaging-guided photodynamic/photothermal/chemodynamic treatment of cervical cancer. *Int J Nanomed*. 2024;19:5837–5858. doi:10.2147/ijn.s466042
22. Singh AV, Alapan Y, Jahnke T, et al. Seed-mediated synthesis of plasmonic gold nanoribbons using cancer cells for hyperthermia applications. *J Mater Chem B*. 2018;6(46):7573–7581. doi:10.1039/c8tb02239a
23. Singh AV, Jahnke T, Wang S, et al. Anisotropic gold nanostructures: optimization via in silico modeling for hyperthermia. *ACS Appl Nano Mater*. 2018;1(11):6205–6216. doi:10.1021/acsanm.8b01406
24. Singh AV, Jungnickel H, Leibrock L, et al. ToF-SIMS 3D imaging unveils important insights on the cellular microenvironment during biomineralization of gold nanostructures. *Sci Rep*. 2020;10(1):261. doi:10.1038/s41598-019-57136-w
25. Jia Y, Sun J, Yang J, et al. Tumor microenvironment-responsive nanoherb delivery system for synergistically inhibition of cancer stem cells. *ACS Appl Mater Interfaces*. 2023;15(13):16329–16342. doi:10.1021/acsami.2c19029

26. Walsh DR, Ross AM, Newport DT, et al. Mechanical characterisation of the human dura mater, falx cerebri and superior sagittal sinus. *Acta Biomater*. 2021;134:388–400. doi:10.1016/j.actbio.2021.07.043
27. Ouyang F, Liu Y, Zhang L, Shuai Q. Hyaluronic acid-targeted dual-bubble/photothermal-driven nanomissile for enhanced "four-in-one" anti-tumor strategy. *Int J Biol Macromol*. 2024;277:133997. doi:10.1016/j.ijbiomac.2024.133997
28. Chen R, Lin X, Tao P, et al. Targeted nanoprobe for magnetic resonance imaging-guided enhanced antitumor via synergetic photothermal/immunotherapy. *J Colloid Interface Sci*. 2025;678(Pt A):937–949. doi:10.1016/j.jcis.2024.08.205
29. Diao Z, Liang Y, Liu Y, et al. Curcumin-enhanced NIR-II-responsive gold nanobipyramids for targeted HSP 90 inhibition. *Mater Today Bio*. 2025;31:101541. doi:10.1016/j.mtbio.2025.101541
30. Abu-Rustum NR, Angioli R, Bailey AE, et al. IGCS Intraoperative Technology Taskforce. Update on near infrared imaging technology: beyond white light and the naked eye, indocyanine green and near infrared technology in the treatment of gynecologic cancers. *Int J Gynecol Cancer*. 2020;30(5):670–683. doi:10.1136/ijgc-2019-001127
31. Liu C, Chang Q, Fan X, et al. Rational construction of CQDs-based targeted multifunctional nanoplatform for synergistic chemo-photothermal tumor therapy. *J Colloid Interface Sci*. 2025;677:79–90. doi:10.1016/j.jcis.2024.08.037
32. Zheng DW, Li B, Li CX, et al. Photocatalyzing CO2 to CO for enhanced cancer therapy. *Adv Mater*. 2017;29(44):1703822. doi:10.1002/adma.201703822
33. Dai Y, Su J, Wu K, et al. Multifunctional thermosensitive liposomes based on natural phase-change material: near-infrared light-triggered drug release and multimodal imaging-guided cancer combination therapy. *ACS Appl Mater Interfaces*. 2019;11(11):10540–10553. doi:10.1021/acsami.8b22748
34. Wang T, Li Z, Lei J, et al. RGD peptide-functionalized micelles loaded with crocetin ameliorate doxorubicin-induced cardiotoxicity. *Int J Pharm X*. 2025;9:100326. doi:10.1016/j.ijpx.2025.100326
35. Huang J, Yang J, Yang Y, et al. Mitigating doxorubicin-induced cardiotoxicity and enhancing anti-tumor efficacy with a metformin-integrated self-assembled nanomedicine. *Adv Sci*. 2025;12(17):e2415227. doi:10.1002/advs.202415227
36. Liu S, Xie S, Sun T, et al. Xinmailong injection ameliorates Doxorubicin-induced cardiotoxicity via the MDH2/OAA pathway. *Phytomedicine*. 2025;145:157010. doi:10.1016/j.phymed.2025.157010
37. Lammers T, Aime S, Hennink WE, Storm G, Kiessling F. Theranostic nanomedicine. *Acc Chem Res*. 2011;44(10):1029–1038. doi:10.1021/ar200019c
38. Liu JMH, Zhang J, Zhang X, et al. Transforming growth factor-beta 1 delivery from microporous scaffolds decreases inflammation post-implant and enhances function of transplanted islets. *Biomaterials*. 2016;80:11–19. doi:10.1016/j.biomaterials.2015.11.065
39. Chen Q, Chen J, Yang Z, et al. Nanoparticle-enhanced radiotherapy to trigger robust cancer immunotherapy. *Adv Mater*. 2019;31(10):e1802228. doi:10.1002/adma.201802228
40. Li P, Wang D, Hu J, Yang X. The role of imaging in targeted delivery of nanomedicine for cancer therapy. *Adv Drug Deliv Rev*. 2022;189:114447. doi:10.1016/j.addr.2022.114447
41. Stöber W, Fink A, Bohn E. Controlled growth of monodisperse silica spheres in the micron size range. *J Colloid Interface Sci*. 1968;26(1):62–69. doi:10.1016/0021-9797(68)90272-5
42. Tang F, Li L, Chen D. Mesoporous silica nanoparticles: synthesis, biocompatibility and drug delivery. *Adv Mater*. 2012;24(12):1504–1534. doi:10.1002/adma.201104763
43. Liu X, Li R, Zhou Y, et al. An all-in-one nanoplatform with near-infrared light promoted on-demand oxygen release and deep intratumoral penetration for synergistic photothermal/photodynamic therapy. *J Colloid Interface Sci*. 2022;608(Pt 2):1543–1552. doi:10.1016/j.jcis.2021.10.082
44. Chou TC. Theoretical basis, experimental design, and computerized simulation of synergism and antagonism in drug combination studies. *Pharmacol Rev*. 2006;58(3):621–681. doi:10.1124/pr.58.3.10
45. Zhang Z, Wang J, Li X, et al. Synergistic effect of pH-sensitive PEGylated RG3-chitosan prodrug nanoparticles encapsulated celastrol on pancreatic cancer. *Drug Deliv*. 2025;32(1):2464189. doi:10.1080/10717544.2025.2464189
46. Liu J, Li RS, Zhang L, et al. Enzyme-activatable polypeptide for plasma membrane disruption and antitumor immunity elicitation. *Small*. 2023;19(24):e2206912. doi:10.1002/smll.202206912
47. Zhang Y, Lv F, Cheng Y, et al. Pd@Au bimetallic nanoplates decorated mesoporous MnO_2 for synergistic nucleus-targeted NIR-II photothermal and hypoxia-relieved photodynamic therapy. *Adv Healthc Mater*. 2020;9(2):e1901528. doi:10.1002/adhm.201901528
48. Cheng M, Yu Y, Huang W, et al. Monodisperse hollow MnO2 with biodegradability for efficient targeted drug delivery. *ACS Biomater Sci Eng*. 2020;6(9):4985–4992. doi:10.1021/acsbiomaterials.0c00507
49. Platas-Iglesias C, Esteban-Gómez D, Helm L, Regueiro-Figueroa M. Transient versus static electron spin relaxation in Mn^{2+} complexes relevant as MRI contrast agents. *J Phys Chem A*. 2016;120(32):6467–6476. doi:10.1021/acs.jpca.6b05423
50. Lu S, Mi Z, Liu P, et al. Repolarizing neutrophils via MnO^2 nanoparticle-activated STING pathway enhances Salmonella-mediated tumor immunotherapy. *J Nanobiotechnology*. 2024;22(1):443. doi:10.1186/s12951-024-02726-8
51. Chen Y, Deng Y, Li Y, et al. Oxygen-independent radiodynamic therapy: radiation-boosted chemodynamics for reprogramming the tumor immune environment and enhancing antitumor immune response. *ACS Appl Mater Interfaces*. 2024;16(17):21546–21556. doi:10.1021/acsami.4c00793